

In Situ Raman Microscopy of Individual $\text{LiNi}_{0.8}\text{Co}_{0.15}\text{Al}_{0.05}\text{O}_2$ Particles in a Li-Ion Battery Composite Cathode

Jinglei Lei, Frank McLarnon, and Robert Kostecki*

Environmental Energy Technologies Division, Lawrence Berkeley National Laboratory, University of California, Berkeley, California 94720

Received: September 2, 2004; In Final Form: October 21, 2004

Kinetic characteristics of Li^+ intercalation/deintercalation into/from individual $\text{LiNi}_{0.8}\text{Co}_{0.15}\text{Al}_{0.05}\text{O}_2$ particles in a composite cathode were studied in situ using Raman microscopy during galvanostatic charge–discharge in 1.2 M LiPF_6 , ethylene carbonate (EC): ethyl methyl carbonate (EMC), 3:7 by volume. Ex situ spectroscopic analysis of a cathode that was removed from a tested high-power Li-ion cell, which suffered substantial power and capacity loss, showed that the state of charge (SOC) of oxide particles on the cathode surface was highly nonuniform despite deep discharge of the Li-ion cell at the end of the test. In situ monitoring of the SOC of selected oxide particles in the composite cathode in a sealed spectro-electrochemical cell revealed that the rate at which particles charge and discharge varied with time and location. The inconsistent kinetic behavior of individual oxide particles was attributed to degradation of the electronically conducting carbon matrix in the composite cathode upon testing. These local microphenomena are most likely responsible for the overall impedance rise of the cathode and contribute to the mechanism of lithium-ion cell failure.

Introduction

A steady degradation of the electrochemical properties of lithium-ion batteries often limits the performance of portable electronic devices and presents a significant barrier for transportation applications such as electric and hybrid-electric vehicles. The mechanism of degradation of various Li-ion battery systems has been the subject of intense studies by many research groups. Arora et al.¹ discussed major detrimental phenomena that lead to capacity fade in lithium-ion cells: (i) electrolyte decomposition under overcharge/overdischarge conditions, (ii) dissolution and/or phase transition of active material in composite cathodes, (iii) surface film formation on electrodes, and (iv) current collector corrosion. Several experimental and theoretical modeling studies showed that formation and development of solid electrolyte interphase (SEI) layers on the cathode and anode is the sole reason for the impedance increase at the positive and negative electrodes.^{2–9}

Lithium-ion intercalation/deintercalation into anode and cathode active material is coupled with electron injection/removal into/from the electrode active material. The impedance growth that is observed at both electrodes is associated with an ion-blocking surface film as well as an electronically insulating barrier formed within the electrode. Thus, the resistances to both ion and electron transfer constitute the overall charge-transfer impedance and contribute to the overall electrode impedance.

Electrode additives such as acetylene black and graphite are used to create conductive pathways within composite cathodes to provide a low-impedance electronic contact between active material particles and the aluminum current collector. The exact amounts of the various composite electrode components, as well as the specific preparation method, are critical for obtaining acceptable electrode and battery performance and are usually determined by a meticulous empirical procedure. Furthermore,

carbon coatings are sometimes applied directly to materials (i.e., not just mixed with them) that exhibit low intrinsic electronic conductivity (e.g., LiFePO_4).^{10,11} Despite the ubiquitous presence of carbon in Li-ion cells, the potential role of the carbonaceous additives in the proposed electrode degradation mechanisms has been so far largely ignored.

Interfacial phenomena occur and manifest themselves at nano or microscale and can be detected and characterized only by techniques of suitable sensitivity and resolution.¹² Raman microscopy mapping of $\text{LiNi}_{0.8}\text{Co}_{0.15}\text{Al}_{0.05}\text{O}_2$ composite cathodes harvested from high-power Li-ion cells showed that the surface distribution of carbon additives in these cathodes changes noticeably upon aging and/or cycling at elevated temperatures and is at least partially responsible for the observed power and capacity loss.¹³ Interestingly, current-sensing atomic force microscopy (AFM) measurements revealed that carbon retreat or redistribution was always accompanied by a dramatic increase in surface electronic resistance in the tested cathodes.

Modern in situ Raman microscopy offers capabilities of collecting information about structure and chemical composition at a spatial resolution of $\sim 2\ \mu\text{m}$. Novak et al. demonstrated the ability of Raman microscopy to investigate the lithium insertion into single particles of the active material in composite cathodes and anodes.^{14,15} Particularly noteworthy is the work of Scherson et al. on embedded single-particle electrodes, in which high-quality Raman scattering spectra were acquired in situ during charge/discharge cycles.^{16,17}

This paper describes an experimental approach that enables us to monitor in situ the spectroscopic behavior of several individual $\text{LiNi}_{0.8}\text{Co}_{0.15}\text{Al}_{0.05}\text{O}_2$ particles in composite cathodes during a galvanostatic charge/discharge cycle. This experimental methodology allows us not only to deconvolute the surface structure and composition of composite cathodes but also detect and characterize Li^+ extraction/injection behavior at micrometer-scale spatial resolution. The results of this study permit us to establish at the particle-size scale a possible link between the

* r_kostecki@lbl.gov.

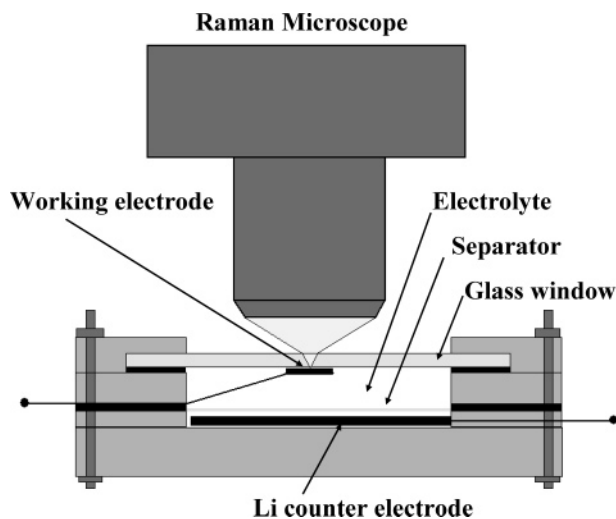


Figure 1. Schematic diagram of the spectro-electrochemical cell employed for in situ Raman microscopy measurements from individual grains and simultaneous electrochemical measurements.

carbon additive retreat/rearrangement phenomenon and the increase of cathode interfacial charge-transfer impedance, which accounts for the observed cell's power and capacity loss during cell testing.

Experimental Section

A schematic diagram of an airtight polyethylene spectro-electrochemical cell is shown in Figure 1. The cell consists of a polyethylene body and a set of gaskets to provide an airtight seal around the electrodes and a glass optical window. The working electrode was prepared by cutting a 1.5-mm wide strip from a $\text{LiNi}_{0.8}\text{Co}_{0.15}\text{Al}_{0.05}\text{O}_2$ composite cathode and removing all electrode material from the Al current collector except for a $\sim 1\text{-mm}^2$ area at the end of the current collector. The active part of the electrode was positioned $\sim 0.2\text{ mm}$ from the glass window, which thereby allowed both electrolyte and optical access to the electrode. The lithium foil counter electrode was fixed at the base of the cell and covered by a piece of commercial Celgard 2300 separator. The cell was assembled in a glovebox, filled with a 1.2-M LiPF_6 + ethylene carbonate + ethyl methyl carbonate (EC/EMC) electrolyte, and then transferred to the Raman microscope experimental setup.

The composite cathode used in this study consisted of $\text{LiNi}_{0.8}\text{Co}_{0.15}\text{Al}_{0.05}\text{O}_2$ (84 wt %), 4 wt % carbon black, 4 wt % SFG-6 graphite, and 8 wt % poly(vinylidene difluoride) (PVDF) binder. The cathodes were manufactured, aged, cycled, and characterized in high-power 18650 Li-ion cells under the ATD Program.¹⁸ In the present study, we compared a fresh cathode (i.e., the electrode that was never in contact with the electrolyte) with a tested cathode removed from a cell that was cycled at 55 °C for 68 weeks and lost 52% of its initial power and 31% of its initial capacity. At the end of cycling, the battery cell was subjected to a discharge cycle, ending at 3.0 V (100% depth of discharge (DOD)). The discharged cell was disassembled in an Ar glovebox. Impedance measurements of the cell components indicated that the $\text{LiNi}_{0.8}\text{Co}_{0.15}\text{Al}_{0.05}\text{O}_2$ cathode was primarily responsible for the observed cell power loss at elevated temperatures. Both fresh and tested cathodes were washed in EMC for 5 min prior to being placed in the spectro-electrochemical cell.

An integrated confocal Raman microscope system Labram made by ISA Groupe Horiba was used to analyze and map the cathode surface structure and composition. The excitation source

was an internal He–Ne (632 nm) 10 mW laser. To avoid local overheating at the sample, the power of the laser beam was adjusted to 0.1 mW with neutral filters of various optical densities. The size of the laser beam at the sample was $\sim 1.2\text{ }\mu\text{m}$ diameter, which is 1 order of magnitude smaller than the size of an average $\text{LiNi}_{0.8}\text{Co}_{0.15}\text{Al}_{0.05}\text{O}_2$ particle, which is actually an agglomerate of smaller submicron crystallites. The average acquisition time for each spectrum was 100 s. The spectra were processed and deconvoluted using the *PeakFit 4.0* commercial software package. Electrochemical measurements were carried out using an EG&G model 362 potentiostat/galvanostat. The charge/discharge current density was $2.3\text{ }\mu\text{A}/\text{mm}^2$, which corresponds to the C/5 rate (i.e., the electrode is charged to its full theoretical capacity within 5 h).

Results and Discussion

Figure 2A shows typical Raman microscopy ex situ spectra of the fresh and tested composite $\text{LiNi}_{0.8}\text{Co}_{0.15}\text{Al}_{0.05}\text{O}_2$ cathodes. The spectra represent a spatial average Raman scattering signal from a $52 \times 75\text{ }\mu\text{m}^2$ area on the cathode surface. The Raman spectra of the composite cathodes are dominated by two groups of bands: a broad maximum centered at $\sim 510\text{ cm}^{-1}$ and two peaks at ~ 1350 and $\sim 1600\text{ cm}^{-1}$. The band at 510 cm^{-1} consists of two Raman-active vibrations characteristic for $\text{LiNi}_{0.8}\text{Co}_{0.15}\text{Al}_{0.05}\text{O}_2$ oxide, which crystallizes in the rhombohedral layered structure of $\alpha\text{-NaFeO}_2$ (*R3m*). The G band at 1600 cm^{-1} corresponds to the E_{2g} active mode of graphite.¹⁹ Small intraplanar (La) and interplanar (Lc) graphite microcrystallite dimensions give rise to the D band at $\sim 1350\text{ cm}^{-1}$, which is assigned to the A_{1g} mode and is associated with the breakage of symmetry that occurs at the edges of graphite sheets. The carbon G and D bands represent graphite and carbon black conducting additives, which are the carbonaceous components of the composite cathode.

The spectrum of the fresh cathode surface shows predominant carbon bands and no signal from the $\text{LiNi}_{0.8}\text{Co}_{0.15}\text{Al}_{0.05}\text{O}_2$, which clearly indicates that the electrode is almost fully coated with carbon additives. The carbon coating is sufficiently thick to prevent detection of the underlying oxide active material.

The cathode surface composition changed significantly upon testing in a battery cell. The spectrum displays a much stronger scattering signal from the oxide relative to the carbon additives, which clearly represents substantial changes in the electrode surface composition that accompanied cell tests. A broad maximum at $\sim 1100\text{ cm}^{-1}$ reveals the presence of lithium fluorophosphates, which originated from the thermal decomposition of the LiPF_6 salt in the electrolyte. These data provide evidence for carbon retreat (or redistribution) from the cathode surface upon cycling and aging at elevated temperatures, and they are in concert with our earlier observations.¹³

Interestingly, the spectra of the tested cathode vary significantly as a function of location on the cathode surface. Figure 2B shows Raman signatures of three separate oxide particles that were probed in situ prior to the spectro-electrochemical measurement. The spectra of all three particles are dominated by a group of bands between 470 and 580 cm^{-1} , characteristic for $\text{Li}_x\text{Ni}_{0.8}\text{Co}_{0.15}\text{Al}_{0.05}\text{O}_2$ oxide and usually associated with vibrations characteristic of the NiO_2 lattice. Typical spectra of fully discharged and fully charged $\text{Li}_{1-x}\text{Ni}_{0.8}\text{Co}_{0.15}\text{Al}_{0.05}\text{O}_2$ cathodes are shown in the Figure 2 insert. The spectrum of the fully discharged oxide consists of a broad peak centered at ca. 500 cm^{-1} and a small sharp peak at 555 cm^{-1} , whereas charged oxide displays two sharp peaks at 475 and 553 cm^{-1} .

The spectral characteristics of the active material in the tested cathode vary strongly as a function of location on the cathode

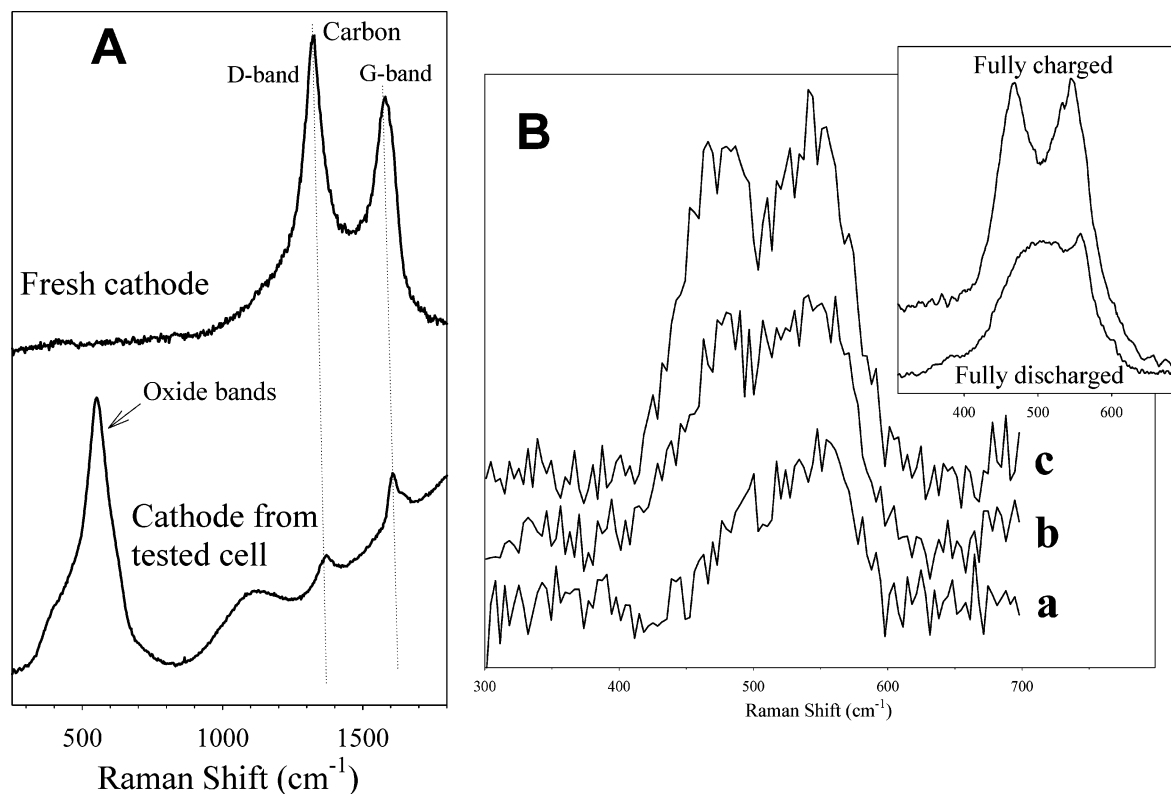


Figure 2. Ex situ average Raman spectra from $52 \times 75 \mu\text{m}^2$ area of the fresh $\text{LiNi}_{0.8}\text{Co}_{0.15}\text{Al}_{0.05}\text{O}_2$ composite cathode and the same cathode removed from a tested high-power Li-ion cell (A). In situ Raman microscope spectra of three individual $\text{LiNi}_{0.8}\text{Co}_{0.15}\text{Al}_{0.05}\text{O}_2$ particles in the tested cathode (B). The band at 510 cm^{-1} consists of two Raman-active vibrations characteristic for $\text{LiNi}_{0.8}\text{Co}_{0.15}\text{Al}_{0.05}\text{O}_2$ oxide; G and D bands at ~ 1600 and 1350 cm^{-1} correspond to E_{2g} and A_{1g} modes of carbon, respectively. The insert shows ex situ Raman spectra of fully charged and fully discharged $\text{LiNi}_{0.8}\text{Co}_{0.15}\text{Al}_{0.05}\text{O}_2$.

surface. The broad peak at 500 cm^{-1} tends to split into two major peaks at 475 and 553 cm^{-1} , which indicates the presence of at least partially charged $\text{Li}_{1-x}\text{Ni}_{0.8}\text{Co}_{0.15}\text{Al}_{0.05}\text{O}_2$. Such a conversion of the band profiles in the vibrational spectra is usually attributed to a change of the a and c parameters of the $\text{Li}_{1-x}\text{Ni}_{0.8}\text{Co}_{0.15}\text{Al}_{0.05}\text{O}_2$ crystal lattice with differing lithium content. Therefore, we can conclude that the cathode surface SOC varies between individual grains of active material from (a) fully discharged through (b) partially charged to (c) fully charged, even though the cell was fully discharged at the end of cell testing.

A sample of the composite cathode from the tested battery was prepared and further studied in the spectro-electrochemical cell shown in Figure 1. Three oxide particles that were selected and investigated by Raman microscopy are shown in the optical image (Figure 3A) of the electrode recorded just prior to the in situ spectro-electrochemical measurement. The Raman microscope was preprogrammed to reposition the laser beam at exactly the same locations to collect a set of three Raman spectra at regular time intervals during the electrochemical measurement. Figure 3B shows the potential versus time response of the tested $\text{LiNi}_{0.8}\text{Co}_{0.15}\text{Al}_{0.05}\text{O}_2$ composite cathode to a galvanostatic charge/discharge cycle at $i = \pm 2.3 \mu\text{A}/\text{mm}^2$. The electrode circuit was opened periodically, and spectra were recorded after the electrode potential relaxed to its equilibrium value (~ 6 min). The cathode was charged from its initial open circuit potential at 3.44 to 4.1 V and then deeply discharged to 2.02 V . A significant IR voltage drop was observed, which originated most likely from the cell geometry and electrode configuration (i.e., (i) the thin electrolyte gap between the electrode and optical window, and (ii) the Li-foil counter-electrode position behind the working electrode).

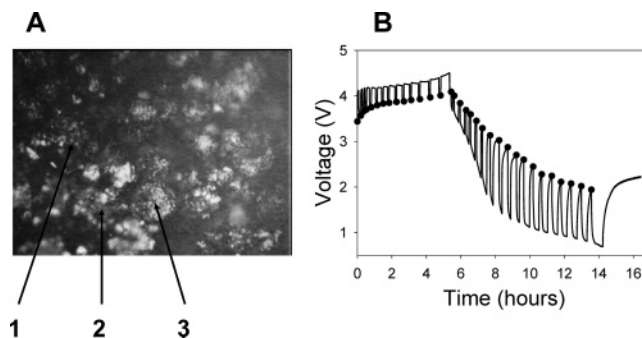


Figure 3. $52 \times 75 \mu\text{m}^2$ optical image of the composite cathode including three individual particles of $\text{LiNi}_{0.8}\text{Co}_{0.15}\text{Al}_{0.05}\text{O}_2$, which were selected for in situ spectral monitoring (A). Galvanostatic charge/discharge curve recorded at $2.3 \mu\text{A}/\text{mm}^2$ (B). Closed circles represent the potential to which the electrode relaxed after the circuit was opened and Raman spectra were collected.

In situ Raman microscopy spectra from three individual particles of $\text{Li}_{1-x}\text{Ni}_{0.8}\text{Co}_{0.15}\text{Al}_{0.05}\text{O}_2$ recorded during the galvanostatic positive-going scan, and the subsequent negative-going scan, are shown in the upper (A) and lower (B) panels in Figure 4, respectively. The broad asymmetric band centered at $\sim 510 \text{ cm}^{-1}$ present in the initial spectra evolves upon charging into two sharp peaks at 475 and 553 cm^{-1} , which are characteristic for the fully charged active material. Importantly, the rate at which the spectra develop is markedly different for each particle. Particles 2 and 3 appear to reach a fully charged state at a much faster rate than particle 1. Similar nonuniform kinetic local behavior was observed during galvanostatic discharge. The SOC of particle 1 changed very little, while the spectra of particles 2 and 3 developed gradually to exhibit spectral features

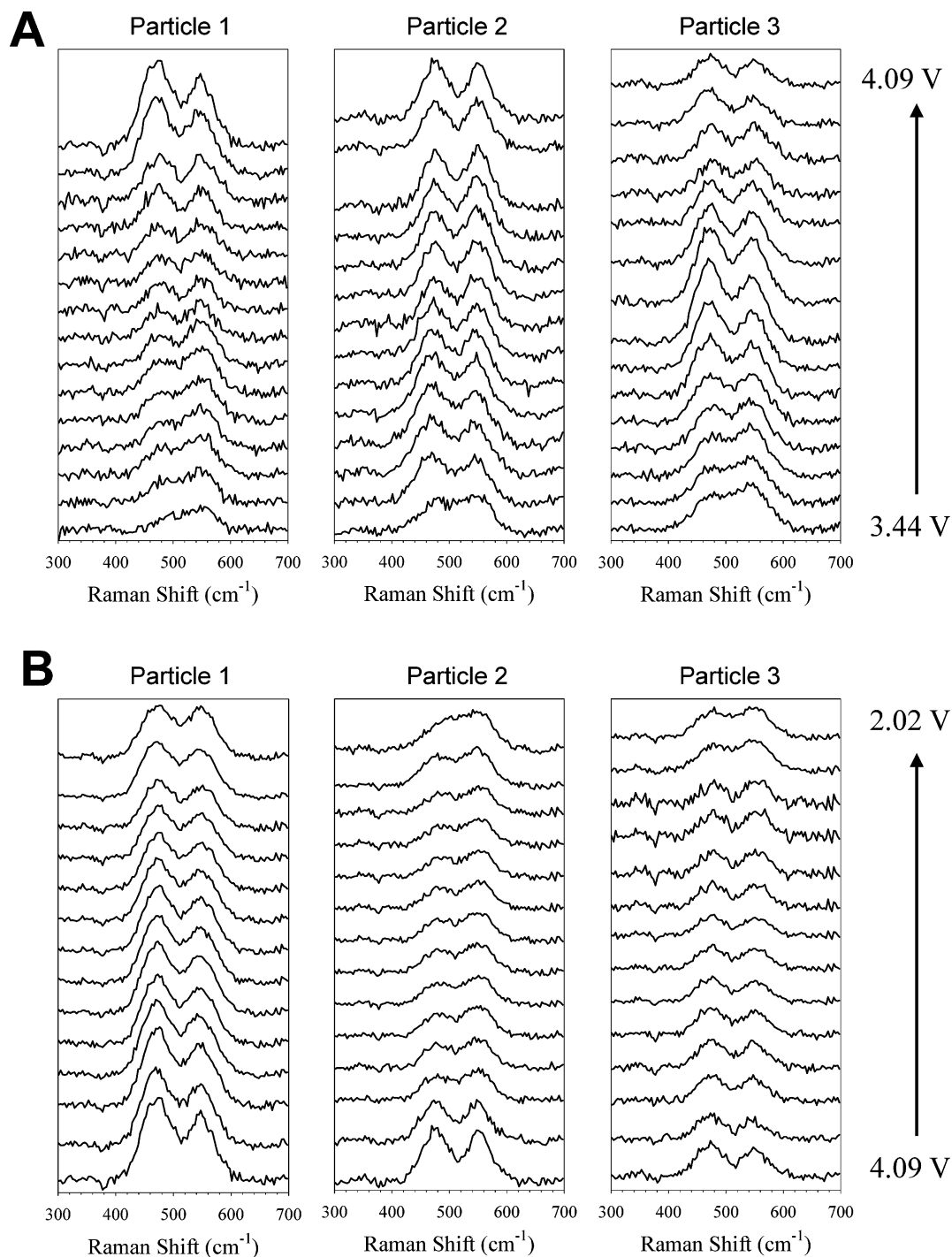


Figure 4. Series of in situ Raman spectra from three individual $\text{LiNi}_{0.8}\text{Co}_{0.15}\text{Al}_{0.05}\text{O}_2$ particles during charging (A) and discharging (B).

characteristic of the fully discharged oxide at the end of the scan. One factor that can explain the observed behavior is that the individual $\text{LiNi}_{0.8}\text{Co}_{0.15}\text{Al}_{0.05}\text{O}_2$ grains in the composite cathode already possess a nonuniform SOC prior to the in situ experiment. On the other hand, the electrochemical charge/discharge cycle did not normalize the oxide particle SOC at the end of scan, despite deep discharge. These observations suggest that kinetic barriers at the microscale exist within the composite cathode. The nonuniform particle SOC during the charge–discharge process indicates that the average potential of the cathode is a mixed potential of individual particles at different states of charge. The particles should eventually equilibrate, unless substantial ionic or electronic resistances exist between particles and/or the Al current collector.

To gain more insight into the kinetic dynamics in the composite cathode at the microscale, we carried out a statistical analysis of all Raman spectra. LiNiO_2 is isostructural with LiCoO_2 , and the Co and Ni atoms in the $\text{Li}_{1-x}\text{Ni}_{1-y}\text{Co}_y\text{O}_2$ lattice occupy equivalent sites in the $R3m$ lattice. The oxidation of Ni ions occurs immediately upon charging and halts at about $x = 0.5$, whereas the oxidation of Co ions continues to $x = 0.8$.²⁰ Al atoms substitute for Ni and Co sites without disturbing the lattice symmetry, and they do not participate in the redox process upon charge/discharge. However, Al substitution enlarges the c -axis parameter and increases the Li^+ diffusion coefficient in the lattice.²¹ A factor group analysis of the $\text{LiNi}_{0.8}\text{Co}_{0.15}\text{Al}_{0.05}\text{O}_2$ lattice predicts two Raman-active vibrations of symmetries A_{1g} and E_g . The main peaks at 475 and 553 cm^{-1} are usually

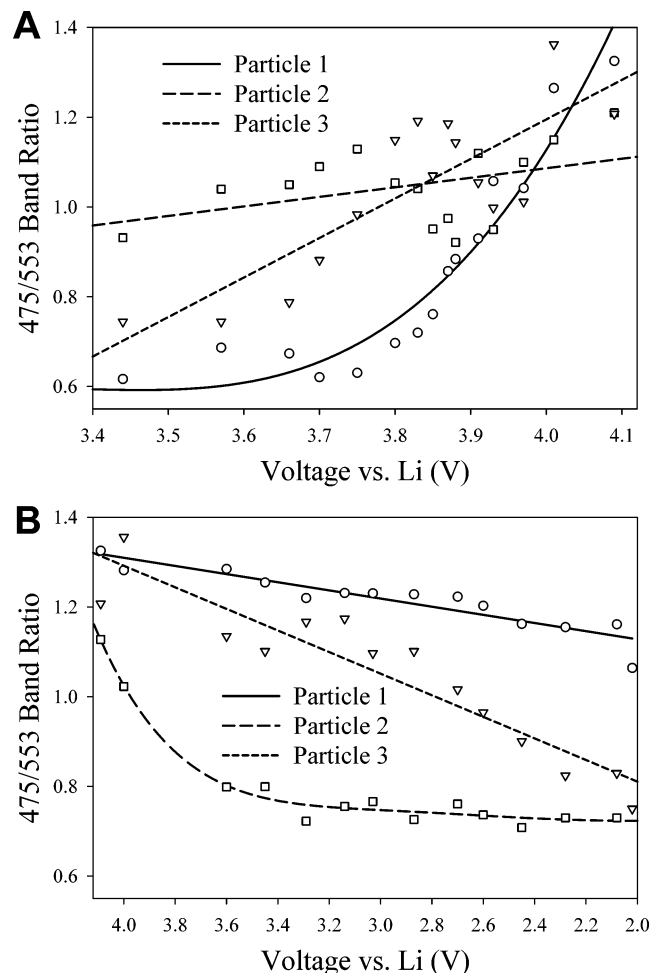


Figure 5. Plots of the 475/553 band ratio deconvoluted and calculated from the Raman spectra of three individual particles shown in Figure 4 during charging (A) and discharging (B).

associated with these in-plane vibrations characteristic of the NiO_2 lattice. The symmetry of A_{1g} and E_g vibrations in the lithiated $\text{LiNi}_{0.8}\text{Co}_{0.15}\text{Al}_{0.05}\text{O}_2$ is somewhat distorted by the presence of electronic and coordination structures originating from weak Li–O bonds. The bands tend to broaden and the 475/553 band ratio decreases significantly with increasing lithium content in the lattice. Thus, the level of lithiation can be monitored by observing and quantifying changes of the 475/553 peak parameters.

A semiquantitative analysis of the cathode surface composition was carried out by deconvoluting Raman spectra into their individual band components. The two major bands at 475 and 553 cm^{-1} were extracted and integrated for each spectrum that was recorded at a given location on the cathode surface. Their ratio was calculated and expressed as a function of the cell voltage (Figure 5). Unfortunately, the precise calibration curve for the 475/553 cm^{-1} band ratio versus voltage was never established for this oxide material. The fresh composite cathode, which we assume offers uniform active material performance at the individual particle level, could not be tested in situ mainly because of the thick carbon coverage and the absence of a signal from the oxide. However, according to our data, we can assume that the integrated 475/553 band ratio is proportional to the lithium content in an individual particle (i.e., a measure of individual particle SOC). On this basis, we can correlate the spectral data collected from individual particles with the electrode average SOC.

Although the plots of the 475/553 band ratio exhibit significant scattering, mainly due to the relatively low signal-to-noise ratio and statistical error of the deconvolution procedure, it is clear that the analyzed particles did charge and discharge at quite different rates. All three particles reached nearly identical SOC upon charging, which is reflected by the very similar 475/553 band ratio of the Raman spectra that were recorded at 4.1 V. However, the rate and profile of SOC versus cell voltage of each particle varied during charging. There is not much change of SOC observed at cell voltages up to 3.7 V for all particles, but at higher cell voltages, particles 1 and 3 charged at a much faster rate than particle 2, which exhibited only a small increase from its original SOC at the end of the charge process. This behavior can be a simple consequence of the fact that all three particles displayed higher original SOC than the average composite cathode SOC. On the other hand, the local ionic and electronic impedance between particles and the rest of the electrode might have also contributed to the observed differences in the electrochemical performance.

Interestingly, the 475/553 band ratio versus cell voltage profile did not exhibit symmetric behavior during the full charge–discharge cycle. Particle 2 displayed a rapid discharge to reach an almost fully discharged state at 3.4 V, and then, no visible change of the 475/553 band ratio was observed. Particles 1 and 3 showed a continuous linear decrease, but neither one reached a fully discharged state despite a very deep discharge to 2 V. Particle 1, in particular, showed very poor performance during the cathode discharge, which is in sharp contrast with its good electrochemical behavior during charging. The changes in the $\text{Li}_{1-x}\text{Ni}_{0.8}\text{Co}_{0.15}\text{Al}_{0.05}\text{O}_2$ crystal lattice c and a parameters upon charging–discharging²² could lead to a loss of mechanical integrity in large agglomerates and poor intergranular contact between primary particles. In extreme cases, such mechanical stress caused by cycling can lead to particle fracture and possible particle isolation.²³

These observations indicate that nonuniform performance at the microscale of the $\text{LiNi}_{0.8}\text{Co}_{0.15}\text{Al}_{0.05}\text{O}_2$ particles in composite cathodes is one of the key signatures of degradation. The nonuniform charge–discharge rate directly implies that the electrode local current distribution is also highly nonhomogeneous. Consequently, some parts of the composite electrode charge and discharge at a much higher rate than the average current indicates, which may lead to local overcharge or overdischarge and thereby trigger other detrimental phenomena such as electrolyte decomposition, structural changes in the oxide, and/or mechanical disintegration of oxide secondary particles. This is consistent with our earlier studies, in which we demonstrated that carbon additive retreat or rearrangement in portions of the tested $\text{LiNi}_{0.8}\text{Co}_{0.15}\text{Al}_{0.05}\text{O}_2$ cathodes is closely linked with reduction in local electronic conductance and is mainly responsible for the observed isolation of oxide active material.¹³ In fact, we did not detect the presence of a surface film that could inhibit lithium-ion diffusion in and out of the oxide. Therefore, partial or complete loss of electronic contact between primary particles of $\text{LiNi}_{0.8}\text{Co}_{0.15}\text{Al}_{0.05}\text{O}_2$ is most likely the origin of the observed electrode impedance increase and nonuniform electrochemical performance of the active material at the microscale.

Carbon additives are uniformly distributed in the fresh composite $\text{LiNi}_{0.8}\text{Co}_{0.15}\text{Al}_{0.05}\text{O}_2$ in the form of a dense matrix, which provides a conductive path not only between large agglomerates and the Al current collector but also between crystallites within the agglomerates. The observed carbon retreat (or possibly carbon redistribution) at the cathode surfaces

uncovers small crystallites within agglomerates and reveals the inherently poor nascent intergranular electronic contact between them. These particles could be in poor electronic contact in the original material, but they could also deteriorate even further during cell cycling/aging. Consequently, the resulting local impedance increase leads to uneven current and potential distribution and excessive current densities at locations that are still in good contact with the conductive carbon matrix. That, in turn, can lead to accelerated degradation of the active material because of local overcharge—overdischarge. We postulate that this chain of detrimental phenomena leads eventually to a substantial loss of electrochemical capacity and power in the composite cathodes despite the fact that cathode active material bulk remains essentially unchanged after testing in Li-ion batteries.

Summary

Local kinetic behavior of individual $\text{LiNi}_{0.8}\text{Co}_{0.15}\text{Al}_{0.05}\text{O}_2$ particles toward Li^+ intercalation—deintercalation in composite cathodes was studied in situ by Raman microscopy during electrochemical charge—discharge cycles in 1.2-M LiPF_6 , EC-EMC, 3:7 by volume. Raman mapping analysis of a cathode that was removed from a tested high-power Li-ion cell, which suffered substantial power and capacity loss, showed that the oxide particle SOC on the cathode surface varied strongly with location despite deep discharge of the Li-ion cell at the end of the test. In situ spectral monitoring of the SOC of selected oxide particles in a composite cathode harvested from a tested cell revealed that the rates at which particles deintercalate—intercalate Li ions changes with time and location. The inconsistent kinetic behavior of the individual oxide particles was attributed to degradation of the electronically conducting matrix in the composite cathode upon testing. These local microphenomena are responsible for uneven performance of the cathode and lead to overall electrode impedance increase and contribute to the mechanism of lithium-ion cell failure.

Acknowledgment. This work was supported by the Director, Office of Energy Research, Office of Basic Energy Sciences, Chemical Sciences Division of the U.S. Department of Energy under contract no. DE-AC03-76SF00098. The authors would

like to thank the Advanced Technology Program for electrode samples and battery testing data.

References and Notes

- (1) Arora, P.; White R. E.; Doyle, M. *J. Electrochem. Soc.* **1998**, *145*, 3647–3667.
- (2) Osaka, T.; Nakade, S.; Rajamäki, M.; Momma, T. *J. Power Sources* **2003**, *119–121*, 929–933.
- (3) Kida, Y.; Kinoshita, A.; Yanagida, K.; Funahashi, A.; Nohma, T.; Yonezu, I. *Electrochim. Acta* **2002**, *47*, 4157–4162.
- (4) Prosini, P. P.; Xia, Y.; Fujieda, T.; Vellone, R.; Shikano, M.; Sakai, T. *Electrochim. Acta* **2001**, *46*, 2623–2629.
- (5) Zhang, D.; Haran, B. S.; Durairajan, A.; White, R. E.; Podrazhansky, Y.; Popov, B. N. *J. Power Sources* **2000**, *91*, 122–129.
- (6) Levi, M. D.; Aurbach, D. *J. Phys. Chem. B* **2004**, *108*, 11693–11703.
- (7) Spotnitz, R. *J. Power Sources* **2003**, *113*, 72–80.
- (8) Christensen, J.; Newman, J. *J. Electrochem. Soc.* **2003**, *150*, A1416–A1420.
- (9) Nobili, F.; Tossici, R.; Marassi, R.; Croce, F.; Scrosati, B. *J. Phys. Chem. B* **2002**, *106*, 3909–3915.
- (10) Ravet, N.; Besner, S.; Simoneau, M.; Valée, A.; Armand, M. U.S. Pat. Appl. 2,270,771, 1999.
- (11) Cushing, B. L.; Goodenough, J. B. *Solid State Sci.* **2002**, *4*, 1487.
- (12) Adams, D. M.; Brus, L.; Chidsey, C. E. D.; Creager, S.; Creutz, C.; Kagan, C. R.; Kamat, P. V.; Lieberman, M.; Lindsay, S.; Marcus, R. A.; Metzger, R. M.; Michel-Beyerle, M. E.; Miller, J. R.; Newton, M. D.; Rolison, D. R.; Sankey, O.; Schanze, K. S.; Yardley, J.; Zhu, X. *J. Phys. Chem. B* **2003**, *107*, 6668–6697.
- (13) Kostecky, R.; McLarnon, F. *Electrochem. Solid State Lett.* **2004**, *7*, A380–A383.
- (14) Novák, P.; Panitz, J.-C.; Joho, F.; Lanz, M.; Imhof, R.; Coluccia, M. *J. Power Sources* **2000**, *90*, 52.
- (15) Panitz, J.-C.; Novák, P. *J. Power Sources* **2001**, *97–98*, 174.
- (16) Totir, D. A.; Scherson, D. A. *Electrochem. Solid State Lett.* **2000**, *3*, 263–265.
- (17) Dokko, K.; Shi, Q.; Stefan, I. C.; Scherson, D. A. *J. Phys. Chem. B* **2003**, *46*, 12549–12554.
- (18) FY 2002 Progress Report for Energy Storage Research and Development, which can be downloaded from the U.S. Department of Energy web site at http://www.eere.energy.gov/vehiclesandfuels/resources/fcvt_publications.shtml
- (19) Tunistra, F.; Koenig, J. L. *J. Chem. Phys.* **1970**, *53*, 1126–1130.
- (20) Nakai, I.; Nakagome, T. *Electrochem. Solid State Lett.* **1998**, *1*, 259.
- (21) Julien, C.; Camacho-Lopez, M. A.; Lemal, M.; Ziolkiewicz, S. *Mater. Sci. Eng.* **2002**, *B95*, 6–13.
- (22) Ronci, F.; Scrosati, B.; Rossi Albertini, V.; P. Perfetti, P. *Electrochem. Solid State Lett.* **2000**, *3*, 174.
- (23) Dokko, K.; Nishizawa, M.; Horikoshi, S.; Itoh, T.; Mohamedi, M.; Uchida, I. *Electrochem. Solid State Lett.* **2000**, *3*, 125.